PCCP

Characterization of the Alkali Metal Oxalates ($MC_2O_4^-$) and their formation by CO_2 reduction via the Alkali Metal Carbonites (MCO_2^-)

Journal:	*Physical Chemistry Chemical Physics*
Manuscript ID	CP-ART-01-2020-000547.R1
Article Type:	Paper
Date Submitted by the Author:	10-Mar-2020
Complete List of Authors:	Jestilä, Joakim; University of Oslo, Department of Chemistry Denton, Joanna; Yale University, Department of Chemistry Perez, Evan; Yale University, Department of Chemistry Khuu, Thien; Yale University, Department of Chemistry Aprà, Edoardo; Pacific Northwest National Lab, EMSL Xantheas, Sotiris; Pacific Northwest National Laboratory, Physical Sciences Division Johnson, Mark; Yale University, Department of Chemistry Uggerud, Einar; University of Oslo, Department of Chemistry

Characterization of the Alkali Metal Oxalates ($MC_2O_4^-$) and their formation by CO_2 reduction via the Alkali Metal Carbonites (MCO_2^-)

Joakim S. Jestilä[1], Joanna K. Denton[2], Evan H. Perez[2], Thien Khuu[2], Edoardo Apra[3], Sotiris S. Xantheas[4,5], Mark A. Johnson[2] and Einar Uggerud[1*]

[1] Department of Chemistry and Hylleraas Centre for Quantum Molecular Sciences, University of Oslo, PO Box 1033, Blindern, Oslo N-0135, Norway

[2] Sterling Chemistry Laboratory, Yale University, New Haven, Connecticut 06520, United States

[3] Environmental Molecular Sciences Laboratory, Pacific Northwest National Laboratory, P.O. Box 999, Richland, Washington 99352, United States

[4] Advanced Computing, Mathematics and Data Division, Pacific Northwest National Laboratory, 902 Battelle Boulevard, P.O. Box 999, MS K1-83, Richland, Washington United States

[5] Department of Chemistry, University of Washington, Seattle, Washington 98195, United States

ABSTRACT

The reduction of carbon dioxide to oxalate has been studied by experimental Collisionally Induced Dissociation (CID) and vibrational characterization of the alkali metal oxalates, supplemented by theoretical electronic structure calculations. The critical step in the reductive process is the coordination of CO_2 to an alkali metal anion, forming a metal carbonite MCO_2^-

able to subsequently add a second CO_2 molecule. While the energetic demand for these reactions is generally low, we find that the degree of activation of CO_2 in terms of charge transfer and transition state energies is the highest for lithium and systematically decreases down the group (M = Li – Cs). This is correlated to the strength of the binding interaction between the alkali metal and CO_2, which can be related to the structure of the oxalate moiety within the product metal complexes evolving from a planar to a staggered conformer with increasing atomic number on the interacting metal. Similar structural changes are observed for crystalline alkali metal oxalates, although the $C_2O_4^{2-}$ moiety is in general more planar in these, a fact that is attributed to the increased number of interacting alkali metal cations compared to the gas-phase ions.

I. INTRODUCTION

While methanol and carbon monoxide are widely used as C1 chemical feedstock, methane and carbon dioxide have found limited uses as of today.[1–4] The utilization of simple molecular building blocks such as CO_2 in direct synthesis is of significant importance, as it has the potential to reduce the waste-to-product ratio of industrial processes by providing a more atom-efficient route to the desired products.[5–9] However, the stability and inertness of CO_2 pose significant challenges in terms of its chemical transformation. Consequently, although it already has various technological and chemical applications[10–13], a significant fraction of these simply release it into the atmosphere in its original state at the end of the process. [14–16] Chemical transformation by reduction of CO_2 to oxalate,

$$2CO_2 + 2e^- \rightarrow C_2O_4^{2-} \tag{1}$$

has received much interest in the recent years. It is most often carried out using oxophilic, electron-poor transition metals or lanthanide complexes.[17–23] This reaction can formally be thought of as either a two-step one-electron reduction, followed by the coupling of the reduced $CO_2^{\bullet-}$ species,

$$2CO_2 + 2e^- \rightarrow 2CO_2^{\bullet-} \quad (2)$$

$$CO_2^{\bullet-} + CO_2^{\bullet-} \rightarrow C_2O_4^{2-}, \quad (3)$$

or alternatively a one-step two-electron reduction followed by nucleophilic attack of CO_2^{2-} on the neutral counterpart,

$$CO_2 + 2e^- \rightarrow CO_2^{2-} \quad (4)$$

$$CO_2^{2-} + CO_2 \rightarrow C_2O_4^{2-}. \quad (5)$$

Carbon dioxide has a negative electron affinity,[24–26] and its reduced intermediates must therefore be stabilized. This can be achieved through interactions with a metal,

$$CO_2 + M^- \rightarrow MCO_2^- \quad (6)$$

$$MCO_2^- + CO_2 \rightarrow MC_2O_4^-. \quad (7)$$

Here, M may represent a metal cathode, as for example in electrochemical reduction,[27–30] a coordinated metal in the case of reduction by organometallic complexes[17–23], or simply a metal atom when isolated as gas-phase species.[31–36] Of particular importance for the reduction reaction in terms of selectivity is the structure and electronic properties of the metal-coordinated CO_2 (Eq. (6)), which constitutes the first intermediate in the formation of a covalent (C—C) bond. CO_2 is a versatile ligand, and several of its coordination modes have been described and characterized.[33–41] Although several recent studies have focused on transition or lanthanide metal catalysts, it has been shown that alkali metal atoms spontaneously reduce CO_2, forming metal–carbon dioxide complexes, $M^+CO_2^-$ and $(M^+)_2CO_2^{2-}$, as well as metal–oxalates, $M^+C_2O_4^-$ and $(M^+)_2C_2O_4^{2-}$.[42–45] The critical step in these reactions is the reduction of CO_2 to $CO_2^{\bullet-}$ by a neutral metal atom. A second metal atom is needed for the reduction to the oxalate dianion. The analogous two-electron reduction of CO_2 to oxalate stimulated by a single alkali metal anion has been studied through the corresponding reverse process, namely the decarboxylation of anionic metal oxalates, $MC_2O_4^-$.[46–48] The MCO_2^- anions formed by decarboxylation of $MC_2O_4^-$ can be formally viewed as complexes between carbonite, CO_2^{2-}, and a singly charged metal cation, M^+, the former assumed to be an important intermediate in the reductive activation of carbon dioxide to carbon monoxide, formic acid, methanol, formaldehyde or other products.[49–51]

The gas-phase oxalate dianion, $C_2O_4^{2-}$, hereafter denoted as Ox^{2-}, is unstable with respect to electron detachment due to Coulombic repulsion, but can be stabilized by a minimum of three water molecules.[52,53] The ion has a C—C single bond in the range 1.54 – 1.57 Å with a rotational barrier of 8 – 25 kJ/mol, depending on the local environment.[54–56] It is widely accepted that the most stable conformer in solution is staggered or slightly twisted, having D_{2d} or D_2/C_2 symmetries, respectively.[54,55,57–61] Similar geometries are adopted by Ox^{2-} when coordinated by metals, as observed in the crystal structures reported in the course of spectroscopic studies of the solid and aqueous alkali metal oxalates, $M_2C_2O_4$, M = Li – Cs.[57,61–65] In general, it is seen that planarity between the alkali metal cations and the oxalate anions in the crystals decreases down the alkali metal group. Thus, the interaction with a suitably polarizing metal, such as the lighter alkali metals Li – K, reduces the Coulombic repulsion between the two carboxylate groups sufficiently to allow for planarity in the oxalate scaffold.[54,55] Alternatively, the degree of planarity can be rationalized by noting that lighter metals fit better within the Ox^{2-} bite and interacts more strongly with the anion.[54,55]

In this study we aim to characterize the structures of alkali metal oxalate complexes, $MC_2O_4^-$, as products of two-electron CO_2 reduction mediated by single metal anions, with particular attention to their connection to the structures of the intermediate metal carbonites, MCO_2^-. In addition, we examine whether the structure of oxalate in the solids is due to a crystal-packing effect, or is intrinsic to the nature of the coordinating ligand. This characterization is achieved by analyzing the results of both cryogenic ion vibrational spectroscopy and CID mass spectrometry with electronic structure calculations. With this joint experimental – theoretical approach, we reveal the factors that control the degree of carbon dioxide activation by the alkali metals.

II. METHODS

a. Mass spectrometry

The formation of the metal oxalate complexes ($MC_2O_4^-$, MOx^-) was accomplished by electrospraying solutions with 1.0 – 4.0 mM oxalic acid and 1.0 – 6.0 mM metal chloride (M = Li, Rb and Cs) or metal hydroxide (M = Na and K). We used a Waters Micromass QTOF 2 MS with a modified custom collision gas inlet for precise control of the collision induced dissociation (CID) conditions. The capillary and time-of-flight detector were operated at 3 and −3 kV, and the multichannel plate detector was kept between 1.9 – 2.3 kV. The source and desolvation temperatures were 100 and 150 C°, respectively. The metal oxalate ions, MOx^-, were mass selected and subjected to CID under 2.0×10^{-4} mbar argon pressure in the collision cell. Breakdown curves were acquired by varying the collision energy during this process and used to estimate the binding energies of the metal oxalates and their metal carbonite fragments. In order to validate the threshold energies estimated by linear extrapolation of the breakdown curves, we applied the same methodology to two systems with well-characterized dissociation thresholds, namely protonated ethanol and deprotonated benzoic acid. Our procedure yields similar values to those reported in the literature.[66–68] More details are available in the Supporting Information (SI). The uncertainties in the threshold energies due to the kinetic and thermal shifts as well as the kinetic energy release associated with the dissociation reactions are difficult to quantify for our experimental setup. For this reason we only report the threshold energies with the numerical uncertainty associated with the extrapolation procedure, ranging from 5 – 45 kJ/mol.

b. Cryogenic ion vibrational spectroscopy

The gas-phase metal oxalate vibrational spectra were obtained using the Yale hybrid Orbitrap/time-of-flight photofragmentation mass spectrometer described previously.[69,70] $M^+Oxalate^{2-}$ (M = Li, Na, K, Rb, Cs) ions were extracted from ~2 mM solutions of oxalic acid and solid metal hydroxide salts (obtained from Sigma Aldrich with no further purification and dissolved in methanol or methanol:H_2O mixtures) using electrospray ionization and mass selected in the quadrupole of a modified[69] Thermo Fisher Scientific Orbitrap Velos Pro. The selected ions were then accumulated in a (20-50 K) Paul trap where they were cooled by a buffer gas mixture of He and (~10%) hydrogen to provide the "messenger tags" (D_2 for Li, K, and Cs; H_2 for Na and Rb) weakly bound to the parent anions. The hydrogen molecules provide a low energy photofragmentation channel, which was monitored to collect linear (i.e., one-photon) vibrational spectra with a minimum of structural perturbation. The spectrum of D-Oxalate was reproduced from a previous report.[71] In that case, a ~1 mM solution of oxalic acid in methanol was electrosprayed and deuterated by leaking D_2O vapor into the second differentially pumped stage before the condensation and photofragmentation of $2H_2$ tags.

c. Computational

We employed the Gaussian 09/16[72] software for the computational studies for the calculations with the B3LYP density functional, the G4 composite method and the second order Møller-Plesset perturbation theory (MP2),[73–77] and the NWChem[78] suite of electronic structure software for the Coupled Cluster Singles and Doubles with a perturbational estimate of triple excitations [CCSD(T)][79–81] calculations. For the MP2 and CCSD(T) calculations, the frozen-core approximation was deemed unsuitable due to certain alkali metal core orbitals being higher in energy than the lowest energy CO_2 valence orbitals in the complexes. This issue has been previously noted by Rassolov and coworkers,[82] as well as Petrie,[83] both suggesting feasible approaches to separate the core from the valence electrons. We chose to rearrange the active space manually on the basis of visual inspection of the orbitals. The frozen core of Na was therefore adjusted to the [$1s^2 2s^2$] electrons and that of K to the [$1s^2 2s^2 2p^6 3s^2$] electrons, see the Supporting Information (SI-C, Figures S17/S18). The Ahlrichs/Weigend basis set def2-TZVPPD was chosen for the calculations due to its versatility and availability over the periodic table (H-Rn), and retrieved from the Basis Set Exchange Web portal.[84–88] For the heavier elements Rb and Cs, this basis set employs effective core potentials (ECP) accounting for scalar relativistic effects through a quasi-relativistic description of the core region.[87–89] The core potentials replace all electrons in the shells up to the penultimate one, i.e. 28 electrons for Rb and 46 electrons for Cs. For the Rb- and Cs-Oxalate complexes, all electrons not described by the effective core potentials were included in the determination of electron correlation. The basis set superposition error was estimated for the metal carbonites using the function counterpoise method,[90–92] that includes the CO_2 deformation energy[93] which is substantial since the CO_2 moiety is bent in the MCO_2^- complexes. A detailed procedure is contained in the SI. The BSSE correction amounts to a correction of 5 – 12 kJ/mol at the CCSD(T) level of theory with the triple-ζ basis set (see Table S5 in the SI). The B3LYP density functional was used for the initial survey of the reaction landscape, while the G4 composite and the CCSD(T) methods were used to refine the thermochemistry, the latter also to provide more reliable metal carbonite geometries.

III. RESULTS AND DISCUSSION

a. Mass spectrometric characterization

The primary fragmentation pathway of all the alkali metal oxalate anions occurs by two sequential decarboxylations, as indicated in Figure 1 and Equations 8 and 9, the first one to produce MCO_2^- and the second M^-,

$$MC_2O_4^- \ (m/z\text{: } 95, 111, 127, 173, 221) \rightarrow MCO_2^- \ (m/z\text{: } 51, 67, 83, 129, 177) + CO_2 \quad (8)$$

$$MCO_2^- \ (m/z\text{: } 51, 67, 83, 129, 177) \rightarrow M^- \ (m/z\text{: } –, 23, 39, 85, 133) + CO_2 \quad (9)$$

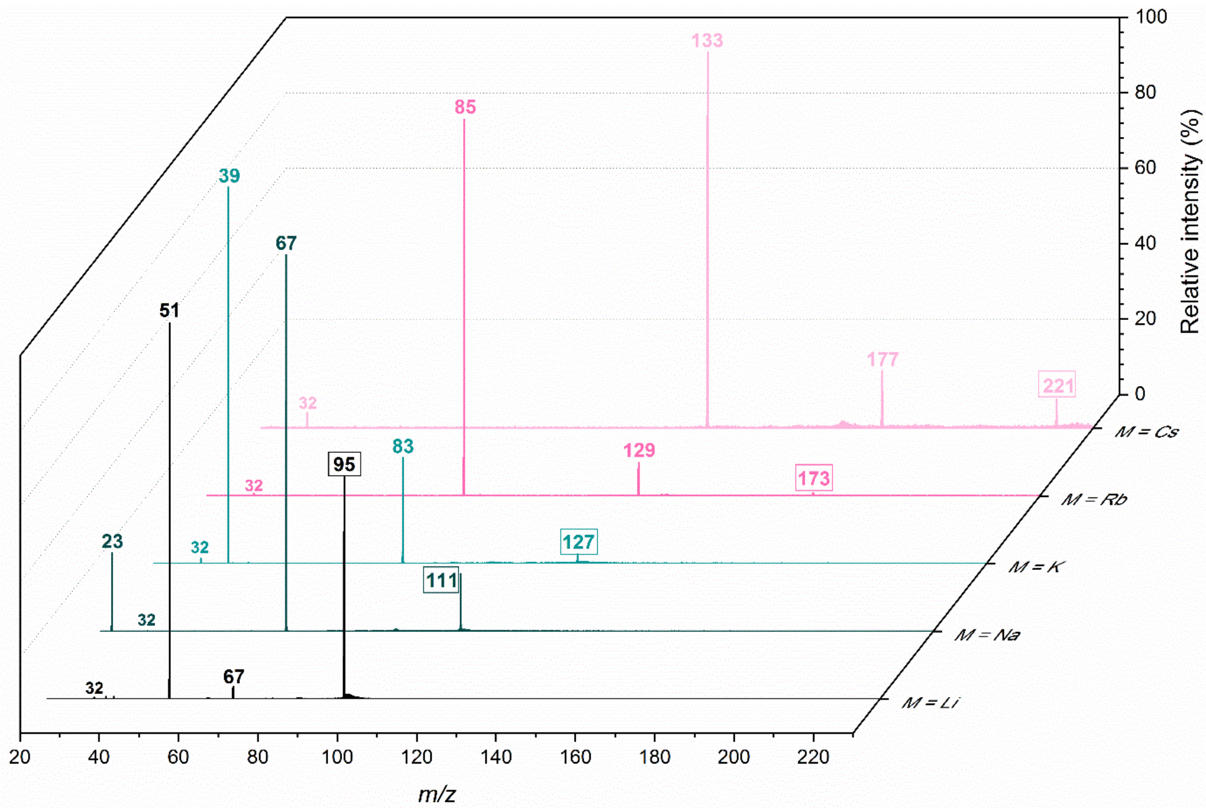

Figure 1. Fragmentation mass spectra of $MC_2O_4^-$ recorded at a collision energy integrated in the range E_{COM} = 3.0 – 5.0 eV under 2.0 × 10^{-4} mbar collision gas (Ar) pressure. The m/z values of the mass selected parent ions are enclosed in frames.

For the lithium oxalate anion, the decarbonylation leading to lithium carbonate, is also observed:

$$LiC_2O_4^- \ (m/z\ 95) \rightarrow LiCO_3^- \ (m/z\ 67) + CO. \qquad (10)$$

These observations are in good agreement with previous reports by Tian,[46] Attygalle[48] and Curtis *et al.*[47] as well as studies of thermal decomposition of the solid alkali metal oxalates.[63,94–97] It should also be mentioned that the lithium anion, Li^- (*m/z* 7) is below the low mass cut-off our QTOF 2 instrument. According to MP2/6-311++G(d,p) calculations by Attygalle *et al.*[48] $LiCO_2^-$ has a lower electron detachment energy (47 kJ/mol) than the decarboxylation barrier (54 kJ/mol), suggesting that electron detachment yielding neutral lithium carbonite radical, which occurs at the crossing of the neutral and ionic surfaces,

$$LiCO_2^- \rightarrow LiCO_2^{\bullet} + e^-, \qquad (11)$$

is the dominant decomposition channel. Our estimates for the electron detachment energy and the decarboxylation barrier of the Li system are 77 kJ/mol and 80 kJ/mol with the G4 composite method and 52 and 69 kJ/mol at the CCSD(T)/def2-TZVPPD level of theory (both using MP2 geometries), respectively. For the sodium analogue, the difference between the computed electron detachment energy and decarboxylation barrier for $NaCO_2^-$ was reported[48] to be 2.5 kJ/mol (67.0 and 69.5 kJ/mol), the former having the lowest energy value. However, Na^- (*m/z* 23) is observed in our experiments. The G4 (using MP2 geometries) results indicate that the vertical electron detachment of $NaCO_2^-$ requires 82 kJ/mol, while the decarboxylation has a barrier of 52 kJ/mol. The CCSD(T) calculations yield values of 67 kJ/mol and 38 kJ/mol for the electron detachment energy and decarboxylation barrier, respectively.

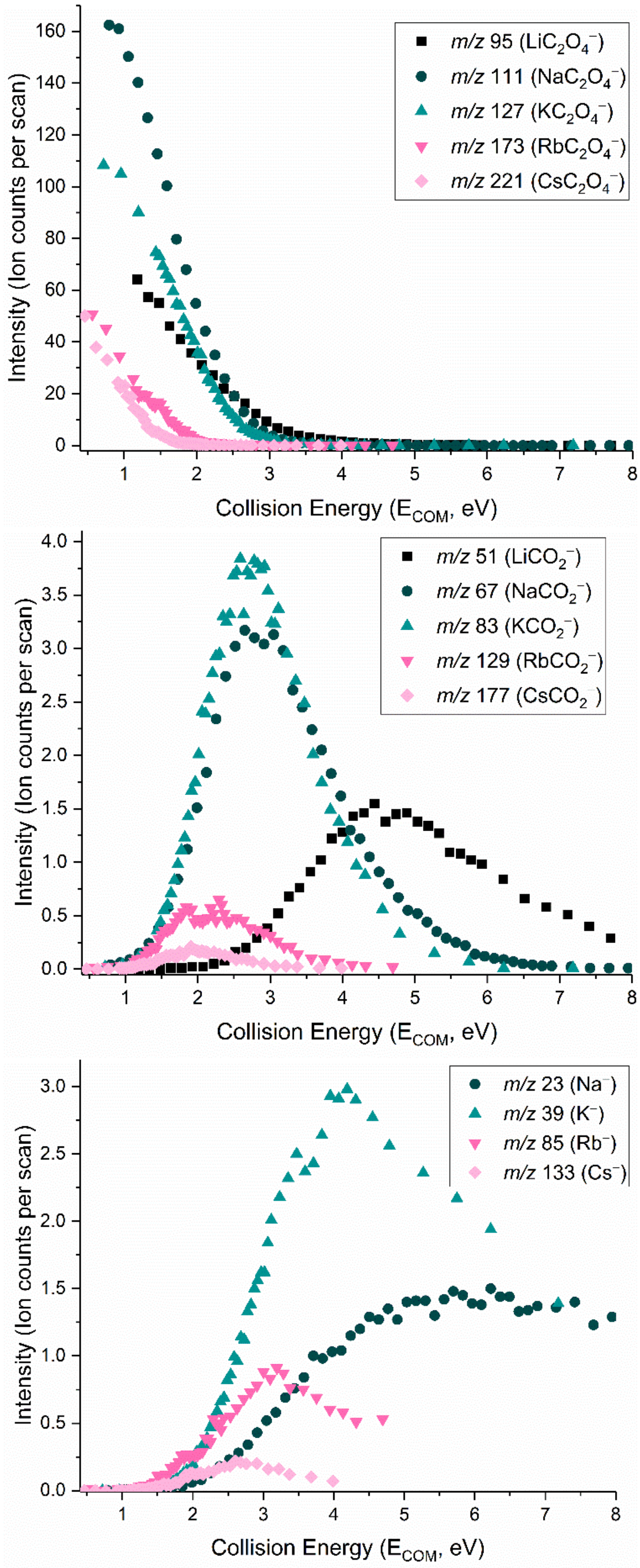

Figure 2. Breakdown curves for the $MC_2O_4^-$ (M = Li, Na, K, Rb, Cs) complexes and appearance curves for MCO_2^- and M^- recorded for the collision energy interval E_{COM} = 0.4 – 8.0 eV under 2.0 × 10^{-4} mbar collision gas (Ar) pressure.

In order to probe the binding energies of the complexes, we measured the breakdown and appearance curves over an energy range from 0.4 – 8.0 eV in the center of mass (COM) frame (Figure 2), and the resulting (estimated) threshold energies are shown in Table 1. It is important to emphasize that the threshold energies are less accurate for M^- than for MCO_2^-, since they are affected by secondary fragmentation. Therefore, we expect a closer correspondence between the theoretical and experimental values for the latter than for the former, given a reliable computational method. To the best of our knowledge, experimental threshold energies have not been reported to date for any of these systems.

Table 1. Experimentally estimated threshold energies for MCO_2^- and M^- in kJ mol^{-1} and MP2/def2-TZVPPD barriers in parentheses. Uncertainties (one standard deviation) are associated with the linear extrapolation procedure outlined in the SI, and only partly reflect the experimental uncertainty (cf. experimental section).

	M = Li	**M = Na**	**M = K**	**M = Rb**	**M = Cs**
MCO_2^-	256 ± 14 (238)	157 ± 10 (150)	150 ± 9 (143)	110 ± 6 (145)	109 ± 11 (158)
M^-	n/a (317)	238 ± 45 (192)	200 ± 19 (176)	157 ± 16 (181)	139 ± 5 (195)

The observation that M^- is increasingly more abundant than MCO_2^- for K, Rb and Cs (cf. Figure 1) can be qualitatively attributed to the decreasing dissociation energy for $MCO_2^- \rightarrow M^- + CO_2$ going down the series from Li to Cs. A more quantitative assessment, however, will require explicit treatment of the electron detachment channel. The combined ion yields of MCO_2^- and M^- do not account for the total signal loss of the precursor oxalate complexes (cf. Figure 2), which could be an artefact of electron detachment. However, a fraction of the total signal loss is inherent to the ion transport, making explicit treatment of the electron detachment channel difficult.

b. Computational modeling of the unimolecular MOx^- dissociation

A detailed computational survey was conducted to aid the understanding of the elementary reaction steps in the dissociation of the alkali metal oxalates into metal anions and carbon dioxide. Some of the key results are presented in Table 2, while more complete potential energy diagrams are reported in the SI. Attygalle *et al.*[48] have previously reported results at the MP2/6-311++G(d,p) level of theory for these reactions, yet several additions and refinements have been made herein, such as employing electronic structure methods of higher accuracy [i.e. CCSD(T) and the G4 composite methods] and using more detailed reaction models. We advise the reader that some of the notation in this Table 2 is introduced in section III d.

Table 2. MP2/def2-TZVPPD and G4, CCSD(T)/def2-TZVPPD (EE + ZPVE) energies for the dissociation of MOx^- in kJ mol^{-1}, relative to $MC_2O_4^-$ (1A). 1A corresponds to the optimum MOx^- geometries, notwithstanding KOx^-. The MOx^- complexes were optimized at the MP2/def2-TZVPPD level of theory and energies were subsequently refined at the CCSD(T)/def2-TZVPPD and G4 levels using these geometries. The MCO_2^- and CO_2 geometries were optimized at both the MP2 and CCSD(T) levels. The G4 energies are computed using the MP2/def2-TZVPPD geometries.

	M = Li	**M = Na**	**M = K**	**M = Rb**	**M = Cs**	**Method**
$MC_2O_4^-$ (1A)	0	0	0	0	0	MP2
	0	0	0	–	–	G4
	0	0	0	0	0	CCSD(T)
$MC_2O_4^-$ (1B)	77	49	−3	–	–	MP2
	76	47	−1	–	–	G4
	76	48	−2	–	–	CCSD(T)
$M(\kappa^2\text{–}O_2C)^-$ (2A) + CO_2	238	150	137	141	154	MP2
	233	161	152	–	–	G4
	237	160	146	152	165	CCSD(T)
$M(\eta^2\text{–}CO_2)^-$ (2B) + CO_2	249	178	161	166	174	MP2
	238	181	172	–	–	G4
	248	180	164	171	183	CCSD(T)

$M^- + 2CO_2$	317	189	169	174	188	MP2
	310	202	189	–	–	G4
	302	183	166	174	189	CCSD(T)
$M + e^- + 2CO_2$	326	211	193	200	216	MP2
	372	255	236	–	–	G4
	346	230	209	216	230	CCSD(T)
EA(M)	9	22	24	26	28	MP2
	63	53	47	–	–	G4
	45	47	43	42	41	CCSD(T)
	60	53	48	46	46	Exp.[98–102]

Our calculations indicate that the energetic demands for the CO_2 loss from MOx^-,

$$MC_2O_4^- \rightarrow MCO_2^- + CO_2, \quad (8)$$

decrease with atomic number on the metal up to KOx^-, and subsequently increase slightly to $CsOx^-$. The same trend is observed for the decarboxylation of MCO_2^-,

$$MCO_2^- \rightarrow M^- + CO_2. \quad (9)$$

This is in contrast to our experimental estimates, the accuracy of which depends on a multitude of factors, which are difficult to assess (cf. experimental section II. a.), making it unfeasible to assign higher validity to either of the experimental or theoretical energies. As a test of the reliability of our computational methods, the electron affinities of the metals were calculated. The experimental Electron Affinities (EA) decrease monotonically down the alkali metal group,[98–102] while MP2 yields an increasing trend down the series. CCSD(T) slightly underestimates the electron affinities of all alkali metals, but manages to reproduce the experimental trend, lithium notwithstanding, while the G4 results are best in agreement with the experimental Electron Affinities (EA) for the Li – K atoms.[98–102, 103–105] Despite erroneous EAs for MP2, there is general qualitative agreement among all methods for the dissociation of MOx^-.

As regards the optimum geometries, the oxalate moiety is twisted from the planar to the staggered conformation with increasing metal atomic number from Li to Cs (Figure 3).

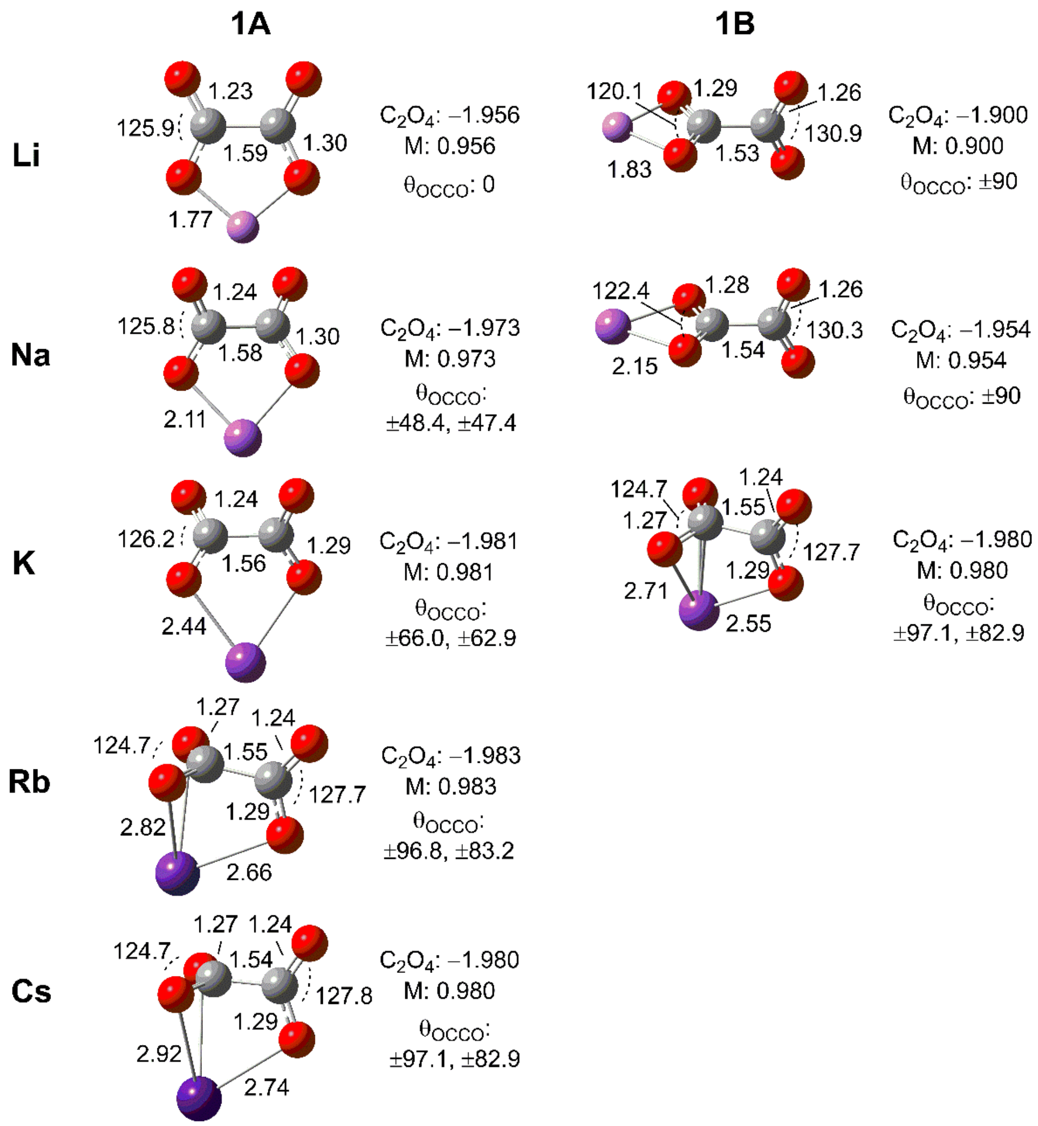

Figure 3. MP2/def2-TZVPPD optimized geometries **1A** and **1B** of the MOx^- complexes with NBO partial charges on C_2O_4 and M indicated. Bond distances in Angstroms (Å), angles in degrees.

Specifically, the lowest energy $LiOx^-$ complex is calculated to be planar (**1A**, C_{2v}), $NaOx^-$ slightly twisted (**1A**, C_2), KOx^- has both twisted (**1A**, C_2) and staggered (i.e., with the metal ion bound closer one -CO_2 group, **1B**, C_s) conformations that are close in energy, while

RbOx⁻ and CsOx⁻ are both staggered (**1A**, C_s), similar to their crystalline counterparts.[57,62–65] The staggered MOx⁻ complexes may dissociate directly to the lowest energy carbonites, **2A**, M(κ^2–O_2C)⁻ (cf. Figure 5), while the planar (LiOx⁻) and twisted (NaOx⁻) complexes require metal migration to yield an end-on isomer (**1B**, C_{2v}) prior to dissociation. For all oxalates, the formation of the **2B** isomers, M(η^2–CO_2) is the most demanding pathway as discussed further in section d.

c. Cryogenic ion vibrational spectroscopic characterization of the MOx⁻ complexes

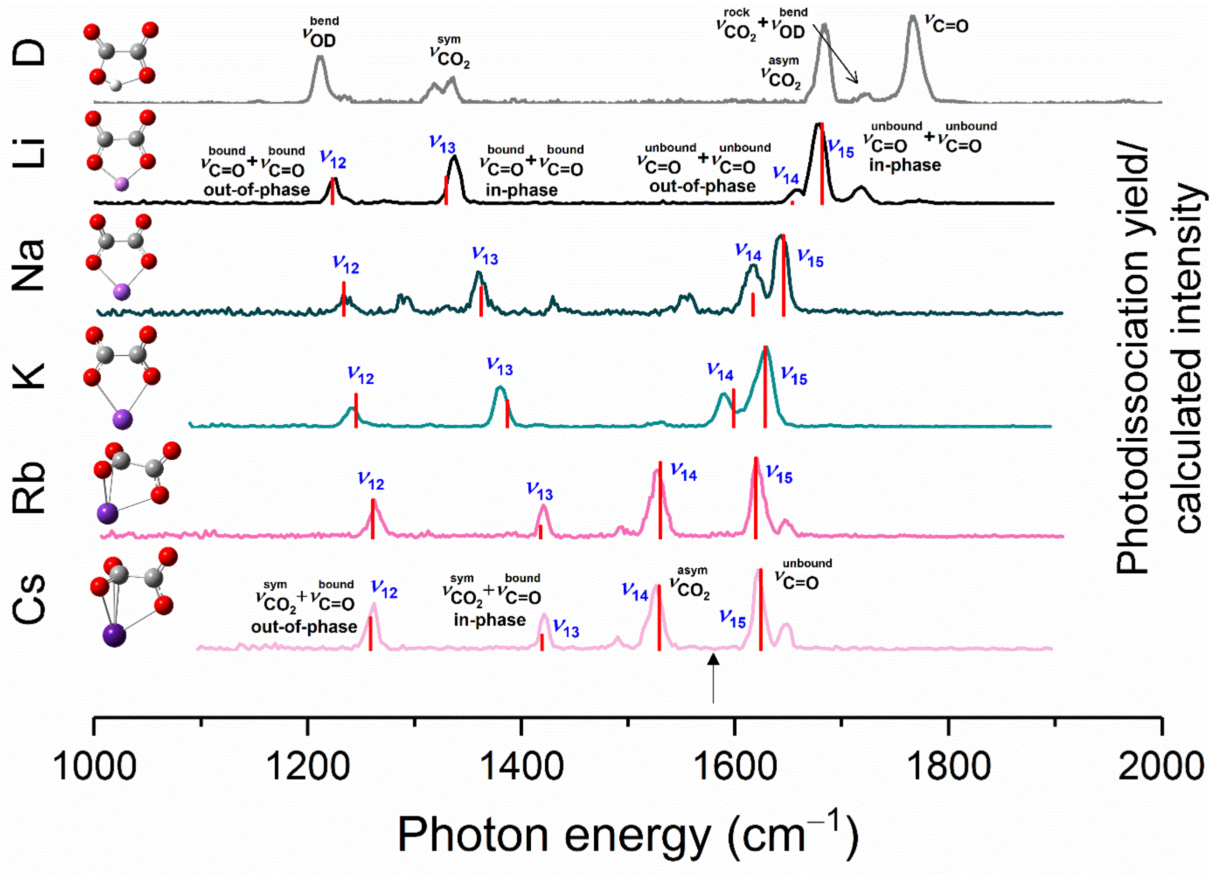

Figure 4. Vibrational predissociation spectra for the $MC_2O_4^-$ (M = D, Li, Na, K, Rb and Cs) complexes "tagged" by either D_2 (M = Li, K and Cs) or H_2 (M = Na and Rb). The deuterium oxalate spectrum is adapted with permission from (Wolke, C. T.; DeBlase, A. F.; Leavitt, C. M.; McCoy, A. B.; Johnson, M. A. Diffuse Vibrational Signature of a Single Proton Embedded in the Oxalate Scaffold, $HO_2CCO_2^-$. *J. Phys. Chem. A* **2015**, *119* (52), 13018–13024.).[71] Copyright (2020) American Chemical Society. The

MP2/def2-TZVPPD minimum energy structures are shown to the left, and the corresponding computed vibrational frequencies (scaled by 0.990 for the Li, Na and K, and by 0.985 for the Rb and Cs), are denoted by sticks. The scaling has been determined according to the best fit to the experimental spectra.

The structural characterization of the alkali metal oxalates was achieved by acquiring vibrational spectra of the corresponding mass-selected, cryogenically cooled gas-phase ions with the results displayed in Figure 4. We could not reach sufficient signal intensities to acquire spectra of the corresponding metal carbonites. The harmonic spectra of the calculated (at the MP2/def2-TZVPPD level of theory) $MC_2O_4^-$ structures feature four transitions in the fingerprint region between 1100 and 1900 cm^{-1}, resulting from combinations of carbonyl (C=O) displacements, which are in good agreement with the experimental band patterns. According to our MP2 calculations, the symmetry of the MOx^- complexes is reduced down the series, from C_{2v} for Li to C_2 for Na and K, and finally C_s for Rb and Cs. Note that for hydrogen/deuterium the point group is also C_s as the potential for proton transfer between O atoms has a double minimum shape.[71]

For the C_{2v} and C_2 metal oxalates (Li, Na and K), the strongest C=O stretching based fundamental is the in-phase combination of the unbound C=O displacements (ν_{15}), observed at 1683, 1652 and 1634 cm^{-1}, respectively. The out-of-phase combinations (ν_{14}) are found slightly lower in energy at 1661, 1625 and 1592 cm^{-1}, and exhibit different shifts relative to the in-phase bands with increasing ligand size ($\Delta\nu$: 22 to 43 cm^{-1}). As expected, the bound C=O displacements are lower in energy, with in-phase combinations (ν_{13}) at 1335, 1358 and 1381 cm^{-1} and out-of-phase combinations (ν_{12}) at 1220, 1232 and 1238 cm^{-1}. Although KOx^- appears well-characterized by a harmonic vibrational model, additional details are recovered from the calculated anharmonic spectra. The FWHM of the unbound C=O fundamental band centered at 1634 cm^{-1} in the K complex is slightly larger with an asymmetrical lineshape relative to the corresponding band for the other metal oxalates (20 cm^{-1} compared to 17 cm^{-1} ($LiOx^{-}$), 15 cm^{-1} ($NaOx^{-}$), 13 cm^{-1} ($RbOx^{-}$) and 11 cm^{-1} ($CsOx^{-}$)). This broadening can be traced to two combination bands with significant oscillator strength (~50 % of the fundamental) within 11 cm^{-1} from the corresponding calculated transition (see SI).

In the asymmetric (C_s) Ox complexes with D, Rb and Cs, the CO_2 moieties are distinguishable from each other. One of these has equivalent C=O bonds, most closely resembling a carboxylate group (CO_2^{-}), while the other has notably different C=O bond lengths, i.e. the structural features of a carboxyl group (M–O–C=O). The strongest oscillator is thus the unbound C=O displacement (ν_{15}) of the carboxyl group, observed at 1768, 1622 and 1626 cm^{-1} for D, Rb and Cs. Nearly as strong is the asymmetric CO_2 displacement of the carboxylate group (ν_{14}), located at 1683 cm^{-1} for the deuterium complex, and at 1528 cm^{-1} for both $RbOx^{-}$ and $CsOx^{-}$. The lowest frequency bands in the range 1200 – 1400 cm^{-1} are due to the in- and out-of-phase combinations of CO_2 bound in a symmetric motif as well as the bound C=O displacements (ν_{13}, ν_{12}). For the deuterium complex, the vibrational modes in this range involve the movement of the deuteron ligand to a higher degree than in the corresponding alkali metal oxalates.[71] Thus, the band at around 1200 cm^{-1} can be mainly attributed to the OD-bend, while the combination of out-of-phase symmetric CO_2 and bound C=O displacement modes make a minor contribution to this feature, consistent with the previous assignment.[71]

In terms of overall trends, we observe a red-shift of the unbound C=O (ν_{14}, ν_{15}) stretches concurrent with the blue-shift of the bound C=O vibrations (ν_{12}, ν_{13}) with increasing metal size. In other words, the bound and unbound C=O displacement bands converge with the increasing atomic number of the metal ligand, a fact that can be attributed to the decreasing covalence in the metal-oxalate bonding. At the same time, oxalate twists towards the most stable staggered configuration of the isolated dianion. For Ox^{2-} the antisymmetric carboxylate stretches are degenerate, with a transition at around 1580 cm^{-1}.[58,60,61] In comparison, we observe a splitting of the corresponding transition (symbolized by an arrow in the Cs trace, to ν_{14} and ν_{15}), due to the presence of the metal in the $RbOx^-$ and $CsOx^-$ spectra in Figure 4. For the Li – K species, this effect manifests itself by the increasing splitting of the unbound C=O modes with metal size, as the out-of-phase mode gradually transforms into the asymmetric CO_2 displacement mode in the $RbOx^-$ and $CsOx^-$ spectra. Note that while the DOx^- spectrum most closely resembles those of $RbOx^-$ and $CsOx^-$, in which oxalate is staggered, the oxalate moiety is planar in that complex. The asymmetry, or rather the non-equivalency of the two CO_2 moieties, are thus enforced by deuteron's smaller size and the double-minimum covalent bonding motif, while the large size of the Rb and Cs ions makes them unsuitable for symmetric accommodation within the oxalate scaffold. Additionally, the increasingly ionic bonding for the heavier alkali metal complexes increases the electron density on the oxalate, which in turn lessens the Coulombic repulsion by twisting about the C—C bond.

The geometry of Ox^{2-} in an aqueous solution with alkali metal counterions was previously studied by Kuroda *et al.*, who proposed the formation of contact ion pairs, $M^+\cdots Ox^{2-}$, in which oxalate assumes D_{2d} and D_{2h} conformations.[61] However, these authors suggested a different position for the metal, with a mixture of side- and end-on coordination being observed, which is likely due to the presence of solvent molecules and the formation of a fully connected hydrogen bonding network in the condensed phase that is absent in the binary complex. We rather find that the gas-phase MOx^- geometries resemble those of the solid metal oxalate salts.[57,62–65] In that regime, however, Ox^{2-} is planar from Li to K, whereas the degree of coplanarity between the alkali metal cations and the oxalate dianion in the crystal lattice decreases with heavier counterions. Crystalline Rb oxalate has two isomeric forms (planar and staggered) with respect to oxalate at elevated temperatures, while in the Cs salt it is staggered.[62,63] The differences in the oxalate conformations between the gas-phase and the solid species could stem from the different numbers of interacting metal cations in the two cases.

Indeed, for the gas-phase $MC_2O_4^-$ complexes, there is only one interacting cation, while the crystalline analogues have several. Thus, we surmise that the structure of oxalate in solid crystals is not solely governed by packing effects as suggested by Dinnebier *et al.*[62], but also by the intrinsic nature of the interaction with the coordinating metal. This is partly supported by noting that the oxalate moiety in both $NaHC_2O4{\bullet}H_2O$[106] and KHC_2O_4[107–109] salts is slightly twisted with an angle of ∠OCCO=13°, and that Ox^{2-} is covalently interacting with a proton in addition to an alkali metal cation.

d. Activation of CO_2 and the formation of the MOx^- complexes

The activation of CO_2 as an isolated molecule can be accomplished by the addition of an alkali metal anion,

$$CO_2 + M^- \rightarrow MCO_2^-. \quad (6)$$

Although a barrier might be present for this reaction, the relevant barrier heights are low (1 – 15 kJ/mol). The addition reaction may lead to two different metal carbonite isomers, one with bidentate oxygen-metal coordination, **2A**, $M(\kappa^2\text{–}O_2C)^-$, the other with mixed carbon-oxygen, or acyl metal coordination, **2B**, $M(\eta^2\text{–}CO_2)^-$. Previous studies have shown that CO_2 forms metalloformates, $M(\eta^1\text{–}CO_2)^-$, with Ni, Cu, Pd, Pt, Au, Ag, and Bi.[31,32,36,110,111] For the alkali metal series, CCSD(T) calculations indicate that only the $LiCO_2^-$ is stable as a metalloformate, with a BDE of 11 kJ/mol and C—M bond of 2.28 Å (not shown). We surmise that the alkali metals attain the bidentate oxygen-metal coordination due to being more oxophilic, as quantified by Kepp[112]. The abovementioned metals are among the least oxophilic (0.0 – 0.2 on the Kepp scale), favoring the metalloformate geometry. Interestingly, Li, has a relatively low oxophilicity (0.3), which could partly explain its increased propensity towards the metalloformate structure.

Formation of the **2B** isomer should occur with the lowest barrier, and we expect it to be the initial product of reaction (6), similarly to what has been reported for the neutral reaction[43–45]

$$CO_2 + M \rightarrow MCO_2. \quad (13)$$

In order to assess the degree of CO_2 reduction in terms of charge transfer, we invoked the natural bond orbital (NBO)[113] analysis at the CCSD(T)/def2-TZVPPD optimized geometries of the metal carbonite anions shown in Figure 5.

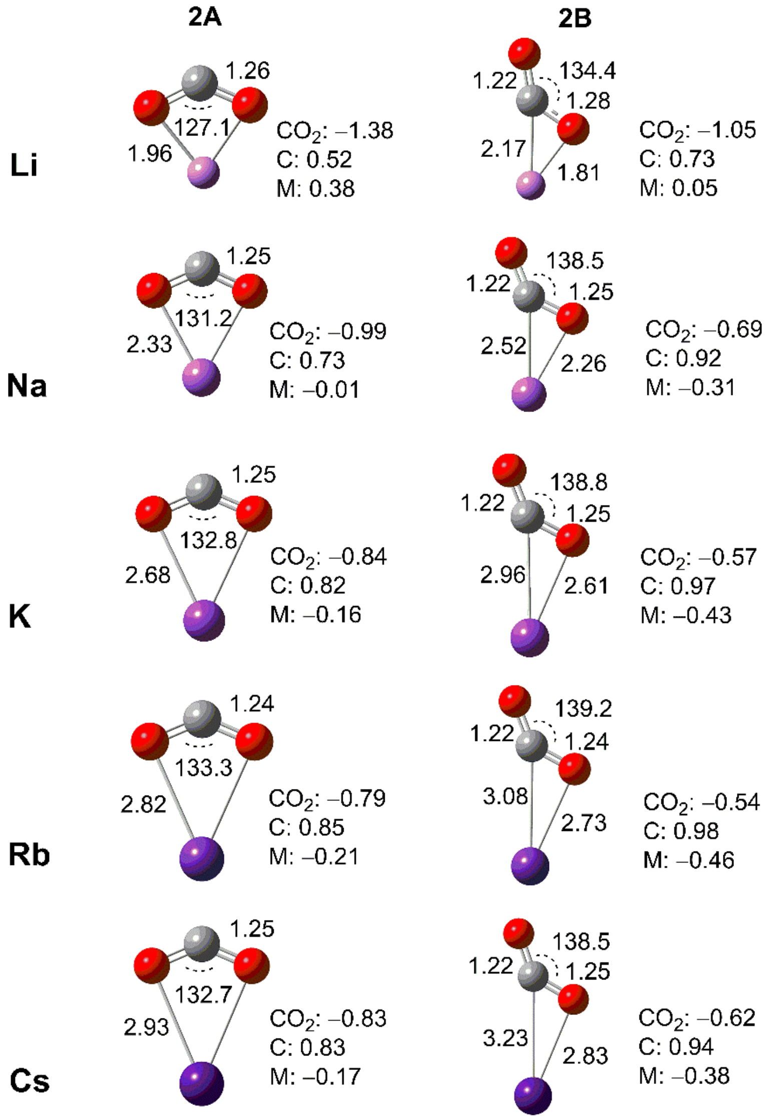

Figure 5. CCSD(T)/def2-TZVPPD optimized geometries of the **2A** ($M(\kappa^2\text{–}O_2C)^-$, C_{2v}) and **2B** ($M(\eta^2\text{–}CO_2)^-$, C_s) alkali metal carbonites. Bond lengths are in Angstroms (Å) and angles in degrees. The NBO partial charges on the CO_2 moiety as well as the carbon and the metal atoms are also indicated.

Going down the series from Li to Cs, the partial charge on the metal atom decreases while it increases on the CO_2 moiety. At the same time, the M—O bond length increases, corresponding to a weaker interaction between CO_2 and M when going from Li to Cs. The ∠OCO bond angle ranges from 127° – 133° in the **2A** isomers, while the corresponding angles for the **2B** isomers are wider, 134° – 139°. These values are close to the reported bond angles for the analogous neutral MCO_2 species.[43,44] The partial charges on the CO_2 in the **2A** complexes are close to −1, suggesting that the electronic state resembles that of the isolated carbon dioxide radical anion, $CO_2^{\bullet-}$.[24] However, due to the metal-oxygen interaction, the C—O bonds are elongated (1.24 – 1.26 Å) and the ∠OCO angle is slightly narrowed when compared to the structure of the isolated $CO_2^{\bullet-}$ (1.23 Å and 138°).[35,114] Thus, the C—O bond lengths of the **2A** complexes range from that of $CO_2^{\bullet-}$ to those found in carboxylate groups (1.26 Å).[115] The **2B** isomers have slightly different C—O bond lengths due to the metal interacting with only one oxygen atom. The largest difference between the two C—O bonds are found in the lithium **2B** isomer, with this difference decreasing down the series from Li to Cs. The second order perturbation theory analysis in the NBO basis suggests that the M—C bond donates electron density to the C—O antibonding orbital, while the oxygen lone pair donates to the M—C antibonding orbital. The stabilization due to the former diminishes with increasing atomic number, while it increases for the latter. This is consistent with the observed C—O bond differences and the elongation of the M—C bond down the series.

The next step in the reduction of CO_2 to $C_2O_4^{2-}$ is the addition of a second carbon dioxide molecule to the metal carbonite,

$$MCO_2^- + CO_2 \rightarrow MC_2O_4^-. \qquad (7)$$

This reaction provides a suitable test system to probe the extent of CO_2 activation in the intermediate MCO_2^- complex. Two phenomenologically different transition states, **TS1A** and **TS2A**, for the addition of a second CO_2 were found, differing according to whether C—C bond formation occurs with or without interaction between the incoming CO_2 and the metal, as shown in Figure 6. The carboxylation of the lightest metal carbonites, Li and Na, is calculated to proceeds exclusively via **TS1A**. Both reaction paths are accessible for the heaviest metal carbonites, K – Cs, with decreasing energetic demands for **TS2A** down the series as discussed further below.

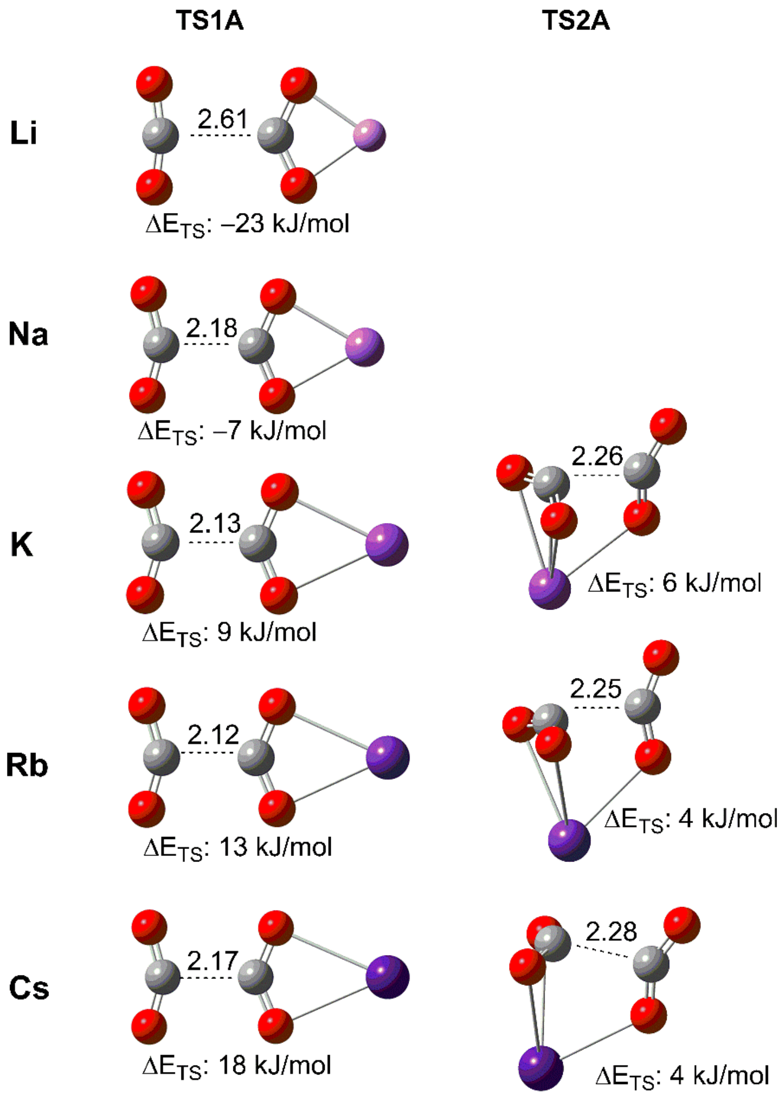

Figure 6. Structures and energetics of transition states for the addition of CO_2 to MCO_2^- (**2A**) at the MP2/def2-TZVPPD level of theory. The C–C bond length (Å) corresponds to the reaction coordinate. ΔE_{TS} is the energy difference (E_e + ZPVE) between the transition state and the MCO_2^- + CO_2 asymptote.

The barrier for CO_2 addition is lowered when the reaction coordinate (primarily the C—C bond length) is elongated towards that of the separated reactants in the transition state. Following this deduction, the metal carbonite becomes a less efficient nucleophile down the alkali metal series, as seen by the decreasing C—C bond length and increasing barrier height in

TS1A. However, the barriers are lowered when the addition proceeds through **TS2A** for the K, Rb and Cs species. We surmise that the energetic penalty is lowered due to the increasingly negative and larger metal participating in the activation of the incoming CO_2. Therefore, we observe mixed carbon and metal nucleophilicity in **TS2A** consistent with the fact that as the metal size increases, more of the negative charge remains on the metal in the MCO_2^- species.

The activation of CO_2 as a carbon nucleophile is more accurately assessed by considering the reaction path via **TS1A** in conjunction with the partial charges on the carbon. The energetic demands increase with metal size for the addition proceeding over this barrier, congruent with the assumption that the lighter metals are more efficient in activating CO_2. We find some support in the literature on the relative reactivities of the neutral lithium and sodium carbonites, MCO_2, in that the latter exhibits lower reactivity towards CO_2 than the former.[45] In addition, we find that the order of reactivities of neutral alkali metals towards CO_2 have been reported as Li > Cs > K > Na.[44] This was rationalized by stating that the initial interaction between CO_2 and the alkali metal leads to the formation of a neutral **2B** analogue, and that its relative stability controls how readily the reaction sequence begins. We find that the interconversion between **2A** and **2B** ions requires less energy than the addition, except for Na. For the **2B** species, carboxylation occurs without a barrier for all metals according to our calculations, and we might expect this reaction to display significant metal activation of the incoming CO_2. This is supported by our calculations predicting a negative charge that is generally larger on the metal and lower on the CO_2 moiety in the **2B** carbonites.

The relative stabilities (in kJ/mol) of the various isomers **1A/1B** and **2A** and the paths connecting them via transition states **TS1A** and **TS2A** for all alkali metals are summarized in Figure 7, which provides a global picture of the potential energy landscape for each system.

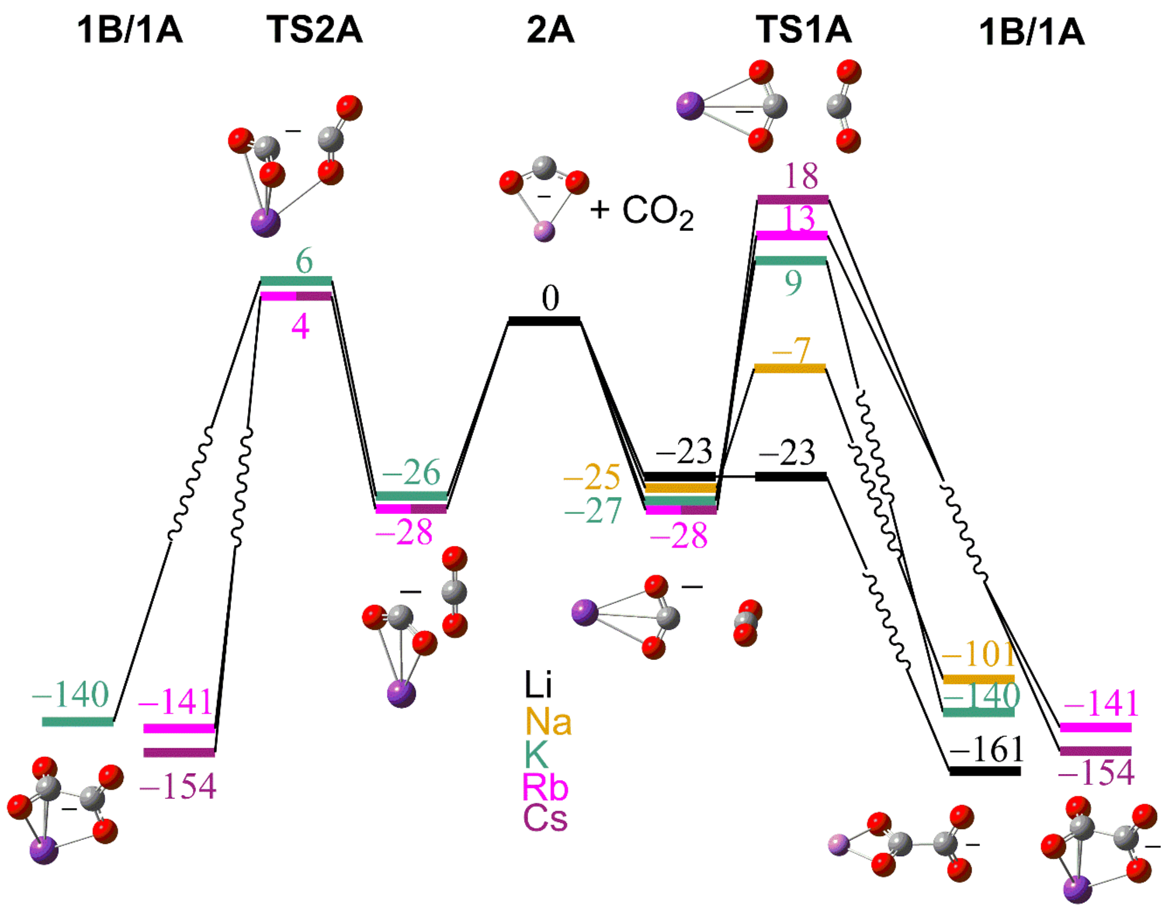

Figure 7. Relative stabilities of isomers **1A/1B** and **2A** (kJ/mol) for the alkali metals considered in this study on the MP2/def2-TZVPPD level of theory.

The core ionization energies, IE(1s), have been shown to correlate with properties such as Lewis acidity and basicity,[116,117] and the C(1s) energies of the MCO_2^- complexes (Table 3) could therefore prove useful descriptors of their carbon nucleophilicity.

Table 3. C(1s) energies (eV) of the MCO_2^- complexes at the CCSD(T)/def2-TZVPPD level of theory. The corresponding value for neutral CO_2 is −311.9 eV.

MCO_2^-	2A	2B
Li	−302.40	−303.861

Na	−304.04	−305.608
K	−304.88	−306.204
Rb	−305.24	−306.487
Cs	−305.20	−306.348

The C(1s) energy is a diagnostic for the charge distribution around the nucleus, and it can be used to infer how well it interacts with positive of negative charges. A higher orbital energy implies more negative charge around the nucleus, favoring nucleophilicity. The near linear correlation (R^2 = 0.96, see SI) of the C(1s) energies with the **2A** + CO_2 (**TS1A**) barrier heights strengthen the results obtained from the NBO analysis. The lower orbital energies of the **2B** species support the assumption that these are not as efficient carbon nucleophiles as **2A**.

Finally, we computed the partial charges on the MOx^- product complexes as a step towards validation of our simple model, where the two electrons needed for the formation of the C–C bond between two CO_2 molecules are provided by the alkali metal anions, as implied by equations (6) and (7). Figure 3 in conjunction with Figure 5 illustrates the expected charge reversal from of the metal −1 to +1 that would result from the stepwise reduction of CO_2 to $C_2O_4^{2-}$.

IV. CONCLUSIONS

Alkali metal oxalate and alkali metal carbonite binding energies decrease down the alkali metal series, as indicated by both approximate experimental dissociation thresholds and the results of electronic structure calculations. For the MOx^- complexes, this trend is evident in the evolution of the C=O stretching fundamentals in the IR spectra, specifically the blueshift of the bound C=O vibrational bands down the series. The size and binding strength of the interacting metal also determines the degree of planarity for the oxalate moiety, which evolves towards the most stable isolated (Ox^{2-}) D_{2d} isomer with increasing metal size. The change in planarity provides an additional transition state for the decarboxylation of the K – Cs alkali metal oxalates, which lead us to propose two different types of nucleophilic reactivity for the intermediate MCO_2^- complexes. These intermediates may react either as pure carbon or mixed carbon-metal centered nucleophiles, with the smaller and more tightly bound metal complexes preferring the former, while those with larger, more polarizable metals favoring the latter. This difference can be attributed to a more complete charge transfer from the metal to the CO_2 moiety in the more tightly bound species (i.e. Li). According to our proposed reaction model, the activation of CO_2 by the alkali metals proceeds energetically downhill when an additional electron is introduced.

CONFLICTS OF INTEREST

There are no conflicts to declare.

ACKNOWLEDGEMENTS

This work was supported by the Norwegian Research Council through Grant No. 249788 (The chemistry of CO_2 activation and fixation) to the Hylleraas Centre for Quantum Molecular Sciences No. 262695/F50 through their Centre of Excellence program, and the Norwegian Supercomputing Program (NOTUR) through a grant of computer time (Grant No. NN4654K). EA and SSX acknowledge support from the Center for Scalable Predictive methods for Excitations and Correlated phenomena (SPEC), which is funded by the U.S. Department of Energy, Office of Science, Basic Energy Sciences, Chemical Sciences, Geosciences and Biosciences Division, as part of the Computational Chemical Sciences Program at Pacific

Northwest National Laboratory. Battelle operates the Pacific Northwest National Laboratory for the U.S. Department of Energy. This research also used computational resources provided by PNNL's Institutional Computing (PIC) and by the National Energy Research Scientific Computing Center, which is supported by the Office of Science of the U.S. Department of Energy under Contract No. DE-AC02-05CH11231. M.A.J. thanks the Air Force Office of Scientific Research (AFOSR) under grants FA9550-17-1-0267 (DURIP) and FA9550-18-1-0213.

AUTHOR INFORMATION

Corresponding Author

*E-mail: einar.uggerud@kjemi.uio.no

ASSOCIATED CONTENT

The Supporting Information contains the following:

SI-A. Mass spectra of oxalic acid and metal chlorides and hydroxides

SI-B. Validation of estimated threshold energies by known reaction energies

SI-C. Molecular orbitals of the alkali metals and metal carbonites

SI-D. Basis set superposition errors with fragment relaxation energy corrections

SI-E. Computational modeling of the unimolecular MOx^- dissociation

SI-F. Relative stabilities of the oxalate dianion conformers in different solvents

SI-G. Alkali metal carbonite (MCO_2^-) C(1s) energies and carboxylation barriers

SI-H. Alkali metal oxalate crystal structures

SI-I. Calculated IR spectra [MP2/def2-TZVPPD] for $MC_2O_4^-$

SI-J. Cartesian coordinates for the MCO_2^- geometries optimized on the [CCSD(T)/def2-TZVPPD] level of theory

SI-K. Cartesian coordinates for [MP2/def2-TZVPPD] optimized species formed during MOx^- dissociation

REFERENCES

(1) Mesters, C. A Selection of Recent Advances in C1 Chemistry. *Annu. Rev. Chem. Biomol. Eng.* **2016**, *7* (1), 223–238. https://doi.org/10.1146/annurev-chembioeng-080615-034616.

(2) Tian, P.; Wei, Y.; Ye, M.; Liu, Z. Methanol to Olefins (MTO): From Fundamentals to Commercialization. *ACS Catal.* **2015**, *5* (3), 1922–1938. https://doi.org/10.1021/acscatal.5b00007.

(3) Klerk, A. de. Fischer–Tropsch Process. In *Kirk-Othmer Encyclopedia of Chemical Technology*; American Cancer Society, 2013; pp 1–20. https://doi.org/10.1002/0471238961.fiscdekl.a01.

(4) Höök, M.; Fantazzini, D.; Angelantoni, A.; Snowden, S. Hydrocarbon Liquefaction: Viability as a Peak Oil Mitigation Strategy. *Philos. Trans. R. Soc. Math. Phys. Eng. Sci.* **2014**, *372* (2006), 20120319. https://doi.org/10.1098/rsta.2012.0319.

(5) Aresta, M.; Dibenedetto, A.; Angelini, A. Catalysis for the Valorization of Exhaust Carbon: From CO_2 to Chemicals, Materials, and Fuels. Technological Use of CO_2. *Chem. Rev.* **2014**, *114* (3), 1709–1742. https://doi.org/10.1021/cr4002758.

(6) Aresta, M.; Dibenedetto, A. Key Issues in Carbon Dioxide Utilization as a Building Block for Molecular Organic Compounds in the Chemical Industry. In *CO_2 Conversion and Utilization*; Song, C., Gaffney, A. F., Fujimoto, K., Eds.; American Chemical Society: Washington, DC, 2002; Vol. 809, pp 54–70.

(7) Plasseraud, L. Carbon Dioxide as Chemical Feedstock. Edited by Michele Aresta. *ChemSusChem* **2010**, *3* (5), 631–632. https://doi.org/10.1002/cssc.201000097.

(8) Quadrelli, E. A.; Centi, G.; Duplan, J.-L.; Perathoner, S. Carbon Dioxide Recycling: Emerging Large-Scale Technologies with Industrial Potential. *ChemSusChem* **2011**, *4* (9), 1194–1215. https://doi.org/10.1002/cssc.201100473.

(9) Sakakura, T.; Choi, J.-C.; Yasuda, H. Transformation of Carbon Dioxide. *Chem. Rev.* **2007**, *107* (6), 2365–2387. https://doi.org/10.1021/cr068357u.

(10) Kolbe, H. Ueber Synthese Der Salicylsäure. *Justus Liebigs Ann. Chem.* **1860**, *113* (1), 125–127. https://doi.org/10.1002/jlac.18601130120.

(11) Schmitt, R.; Burkard, E. *Ber Dtsch Chem Ges* **1877**, *20*, 2699.

(12) Carl, B.; Wilhelm, M. Process of Manufacturing Urea. US1429483A, September 19, 1922.

(13) Ernest Solvay. US263981A, September 5, 1882.

(14) Aresta, M.; Dibenedetto, A.; Dutta, A. Energy Issues in the Utilization of CO_2 in the Synthesis of Chemicals: The Case of the Direct Carboxylation of Alcohols to Dialkyl-Carbonates. *Catal. Today* **2017**, *281*, 345–351. https://doi.org/10.1016/j.cattod.2016.02.046.

(15) Aresta, M.; Dibenedetto, A.; Angelini, A. The Changing Paradigm in CO2 Utilization. *J. CO2 Util.* **2013**, *3–4*, 65–73. https://doi.org/10.1016/j.jcou.2013.08.001.

(16) Zhu, Q. Developments on CO2-Utilization Technologies. *Clean Energy* **2019**, *3* (2), 85–100. https://doi.org/10.1093/ce/zkz008.

(17) Pokharel, U. R.; Fronczek, F. R.; Maverick, A. W. Reduction of Carbon Dioxide to Oxalate by a Binuclear Copper Complex. *Nat. Commun.* **2014**, *5* (1), 1–5. https://doi.org/10.1038/ncomms6883.

(18) Paparo, A.; Silvia, J. S.; Kefalidis, C. E.; Spaniol, T. P.; Maron, L.; Okuda, J.; Cummins, C. C. A Dimetalloxycarbene Bonding Mode and Reductive Coupling Mechanism for Oxalate Formation from CO_2. *Angew. Chem. Int. Ed.* **2015**, *54* (31), 9115–9119. https://doi.org/10.1002/anie.201502532.

(19) Willauer, A. R.; Toniolo, D.; Fadaei-Tirani, F.; Yang, Y.; Laurent, M.; Mazzanti, M. Carbon Dioxide Reduction by Dinuclear Yb(II) and Sm(II) Complexes Supported by Siloxide Ligands. *Dalton Trans.* **2019**, *48* (18), 6100–6110. https://doi.org/10.1039/C9DT00554D.

(20) Formanuik, A.; Ortu, F.; Inman, C. J.; Kerridge, A.; Castro, L.; Maron, L.; Mills, D. P. Concomitant Carboxylate and Oxalate Formation From the Activation of CO_2 by a Thorium(III) Complex. *Chem. Weinh. Bergstr. Ger.* **2016**, *22* (50), 17976–17979. https://doi.org/10.1002/chem.201604622.

(21) Farrugia, L. J.; Lopinski, S.; Lovatt, P. A.; Peacock, R. D. Fixing Carbon Dioxide with Copper: Crystal Structure of $[LCu(\mu\text{-}C_2O_4)CuL][Ph_4B]_2$ (L = N,N‘,N‘ ‘-Triallyl-1,4,7-Triazacyclononane). *Inorg. Chem.* **2001**, *40* (3), 558–559. https://doi.org/10.1021/ic000418y.

(22) Tanaka, K.; Kushi, Y.; Tsuge, K.; Toyohara, K.; Nishioka, T.; Isobe, K. Catalytic Generation of Oxalate through a Coupling Reaction of Two CO_2 Molecules Activated

on [(Ir(η^5-C_5Me_5))$_2$(Ir((η^4-C_5Me_5)CH_2CN)(μ^3-S)$_2$]. *Inorg. Chem.* **1998**, *37* (1), 120–126. https://doi.org/10.1021/ic9702328.

(23) Horn, B.; Limberg, C.; Herwig, C.; Braun, B. Nickel(I)-Mediated Transformations of Carbon Dioxide in Closed Synthetic Cycles: Reductive Cleavage and Coupling of CO_2 Generating $Ni^{I}CO$, $Ni^{II}CO_3$ and $Ni^{II}C_2O_4Ni^{II}$ Entities. *Chem. Commun.* **2013**, *49* (93), 10923–10925. https://doi.org/10.1039/C3CC45407J.

(24) Schröder, D.; Schalley, C. A.; Harvey, J. N.; Schwarz, H. On the Formation of the Carbon Dioxide Anion Radical $CO_2^{\cdot-}$ in the Gas Phase. *Int. J. Mass Spectrom.* **1999**, *185*, 25–35.

(25) Gutsev, G. L.; Bartlett, R. J.; Compton, R. N. Electron Affinities of CO2, OCS, and CS2. *J. Chem. Phys.* **1998**, *108* (16), 6756–6762. https://doi.org/10.1063/1.476091.

(26) Compton, R. N.; Reinhardt, P. W.; Cooper, C. D. Collisional Ionization of Na, K, and Cs by CO_2, COS, and CS_2: Molecular Electron Affinities. *J. Chem. Phys.* **1975**, *63* (9), 3821. https://doi.org/10.1063/1.431875.

(27) Chernyshova, I. V.; Somasundaran, P.; Ponnurangam, S. On the Origin of the Elusive First Intermediate of CO_2 Electroreduction. *Proc. Natl. Acad. Sci.* **2018**, *115* (40), E9261–E9270. https://doi.org/10.1073/pnas.1802256115.

(28) Hori, Y. Electrochemical CO_2 Reduction on Metal Electrodes. In *Modern Aspects of Electrochemistry*; Vayenas, C. G., White, R. E., Gamboa-Aldeco, M. E., Eds.; Modern Aspects of Electrochemistry; Springer: New York, NY, 2008; pp 89–189. https://doi.org/10.1007/978-0-387-49489-0_3.

(29) Feaster, J. T.; Shi, C.; Cave, E. R.; Hatsukade, T.; Abram, D. N.; Kuhl, K. P.; Hahn, C.; Nørskov, J. K.; Jaramillo, T. F. Understanding Selectivity for the Electrochemical Reduction of Carbon Dioxide to Formic Acid and Carbon Monoxide on Metal

Electrodes. *ACS Catal.* **2017**, *7* (7), 4822–4827. https://doi.org/10.1021/acscatal.7b00687.

(30) Akhade, S. A.; Luo, W.; Nie, X.; Asthagiri, A.; Janik, M. J. Theoretical Insight on Reactivity Trends in CO_2 Electroreduction across Transition Metals. *Catal. Sci. Technol.* **2016**, *6* (4), 1042–1053. https://doi.org/10.1039/C5CY01339A.

(31) Thompson, M. C.; Ramsay, J.; Weber, J. M. Solvent-Driven Reductive Activation of CO2 by Bismuth: Switching from Metalloformate Complexes to Oxalate Products. *Angew. Chem. Int. Ed.* **2016**, *55* (48), 15171–15174. https://doi.org/10.1002/anie.201607445.

(32) Knurr, B. J.; Weber, J. M. Solvent-Mediated Reduction of Carbon Dioxide in Anionic Complexes with Silver Atoms. *J. Phys. Chem. A* **2013**, *117* (41), 10764–10771. https://doi.org/10.1021/jp407646t.

(33) Ricks, A. M.; Brathwaite, A. D.; Duncan, M. A. IR Spectroscopy of Gas Phase V(CO2)N+ Clusters: Solvation-Induced Electron Transfer and Activation of CO2. *J. Phys. Chem. A* **2013**, *117* (45), 11490–11498. https://doi.org/10.1021/jp4089035.

(34) Miller, G. B. S.; Esser, T. K.; Knorke, H.; Gewinner, S.; Schöllkopf, W.; Heine, N.; Asmis, K. R.; Uggerud, E. Spectroscopic Identification of a Bidentate Binding Motif in the Anionic Magnesium-CO_2 Complex ($[ClMgCO_2]^-$). *Angew. Chem.* **2014**, *126* (52), 14635–14638. https://doi.org/10.1002/ange.201409444.

(35) Blaziak, K.; Tzeli, D.; Xantheas, S. S.; Uggerud, E. The Activation of Carbon Dioxide by First Row Transition Metals (Sc–Zn). *Phys. Chem. Chem. Phys.* **2018**, *20* (39), 25495–25505. https://doi.org/10.1039/C8CP04231D.

(36) Lim, E.; Kim, S. K.; Bowen, K. H. Photoelectron Spectroscopic and Computational Study of $(M–CO_2)^-$ Anions, M = Cu, Ag, Au. *J. Chem. Phys.* **2015**, *143* (17), 174305. https://doi.org/10.1063/1.4935061.

(37) Freund, H.-J.; Messmer, R. P. On the Bonding and Reactivity of CO_2 on Metal Surfaces. *Surf. Sci. Lett.* **1986**, *172* (1), A333. https://doi.org/10.1016/0167-2584(86)91274-0.

(38) Aresta, M.; Angelini, A. The Carbon Dioxide Molecule and the Effects of Its Interaction with Electrophiles and Nucleophiles. In *Carbon Dioxide and Organometallics*; Lu, X.-B., Ed.; Topics in Organometallic Chemistry; Springer International Publishing: Cham, 2016; pp 1–38. https://doi.org/10.1007/3418_2015_93.

(39) Gibson, D. H. Carbon Dioxide Coordination Chemistry: Metal Complexes and Surface-Bound Species. What Relationships? *Coord. Chem. Rev.* **1999**, *185–186*, 335–355. https://doi.org/10.1016/S0010-8545(99)00021-1.

(40) Barwa, E.; Ončák, M.; Pascher, T. F.; Herburger, A.; Linde, C. van der; Beyer, M. K. Infrared Multiple Photon Dissociation Spectroscopy of Hydrated Cobalt Anions Doped with Carbon Dioxide CoCO2(H2O)N−, N=1–10, in the C−O Stretch Region. *Chem. – Eur. J.* **2020**, *26* (5), 1074–1081. https://doi.org/10.1002/chem.201904182.

(41) Thomas, D. A.; Mucha, E.; Gewinner, S.; Schöllkopf, W.; Meijer, G.; von Helden, G. Vibrational Spectroscopy of Fluoroformate, FCO2–, Trapped in Helium Nanodroplets. *J. Phys. Chem. Lett.* **2018**, *9* (9), 2305–2310. https://doi.org/10.1021/acs.jpclett.8b00664.

(42) Jacox, M. E.; Milligan, D. E. Vibrational Spectrum of CO_2^- in an Argon Matrix. *Chem. Phys. Lett.* **1974**, *28* (2), 163–168. https://doi.org/10.1016/0009-2614(74)80043-6.

(43) Kafafi, Z. H.; Hauge, R. H.; Billups, W. E.; Margrave, J. L. Carbon Dioxide Activation by Lithium Metal. 1. Infrared Spectra of Lithium Carbon Dioxide ($Li^+CO_2^-$), Lithium Oxalate ($Li^+C_2O_4^-$), and Lithium Carbon Dioxide ($Li_2^{2+}CO_2^{2-}$) in Inert-Gas Matrices. *J. Am. Chem. Soc.* **1983**, *105* (12), 3886–3893. https://doi.org/10.1021/ja00350a025.

(44) Kafafi, Z. H.; Hauge, R. H.; Billups, W. E.; Margrave, J. L. Carbon Dioxide Activation by Alkali Metals. 2. Infrared Spectra of $M^+CO_2^-$ and $M_2^{2+}CO_2^{2-}$ in Argon and Nitrogen Matrixes. *Inorg. Chem.* **1984**, *23* (2), 177–183. https://doi.org/10.1021/ic00170a013.

(45) Manceron, L.; Loutellier, A.; Perchard, J. P. Reduction of Carbon Dioxide to Oxalate by Lithium Atoms: A Matrix Isolation Study of the Intermediate Steps. *J. Mol. Struct.* **1985**, *129* (1), 115–124. https://doi.org/10.1016/0022-2860(85)80197-6.

(46) Tian, Z.; Chan, B.; Sullivan, M. B.; Radom, L.; Kass, S. R. Lithium Monoxide Anion: A Ground-State Triplet with the Strongest Base to Date. *Proc. Natl. Acad. Sci.* **2008**, *105* (22), 7647–7651. https://doi.org/10.1073/pnas.0801393105.

(47) Curtis, S.; Renaud, J.; Holmes, J. L.; Mayer, P. M. Old Acid, New Chemistry. Negative Metal Anions Generated from Alkali Metal Oxalates and Others. *J. Am. Soc. Mass Spectrom.* **2010**, *21* (11), 1944–1946. https://doi.org/10.1016/j.jasms.2010.08.003.

(48) Attygalle, A. B.; Axe, F. U.; Weisbecker, C. S. Mild Route to Generate Gaseous Metal Anions. *Rapid Commun. Mass Spectrom.* **2011**, *25* (6), 681–688. https://doi.org/10.1002/rcm.4913.

(49) Paparo, A.; Okuda, J. Carbonite, the Dianion of Carbon Dioxide and Its Metal Complexes. *J. Organomet. Chem.* **2018**, *869*, 270–274. https://doi.org/10.1016/j.jorganchem.2017.10.005.

(50) Miller, G. B. S.; Uggerud, E. C−C Bond Formation of Mg- and Zn-Activated Carbon Dioxide. *Chem. – Eur. J.* **2018**, *24* (18), 4710–4717. https://doi.org/10.1002/chem.201706069.

(51) Dossmann Soldi-Lose, H.; Afonso, C.; Lesage, D.; Tabet, J.-C.; Uggerud, E. Formation and Characterization of Gaseous Adducts of Carbon Dioxide to Magnesium, $(CO_2)MgX^-$ (X=OH, Cl, Br). *Angew. Chem. Int. Ed.* **2012**, *51* (28), 6938–6941. https://doi.org/10.1002/anie.201108477.

(52) Wang, X.-B.; Yang, X.; Nicholas, J. B.; Wang, L.-S. Photodetachment of Hydrated Oxalate Dianions in the Gas Phase, $C_2O_4^{2-}(H_2O)_n$ (N=3–40): From Solvated Clusters to Nanodroplet. *J. Chem. Phys.* **2003**, *119* (7), 3631–3640. https://doi.org/10.1063/1.1590641.

(53) Yang, X.; Wang, X.-B.; Wang, L.-S. Photodetachment of Hydrated Sulfate Doubly Charged Anions: $SO_4^{2-}(H_2O)_n$ (n = 4−40)†. *J. Phys. Chem. A* **2002**, *106* (33), 7607–7616. https://doi.org/10.1021/jp014632z.

(54) Dewar, M. J. S.; Zheng, Y.-J. Structure of the Oxalate Ion. *J. Mol. Struct. THEOCHEM* **1990**, *209* (1–2), 157–162. https://doi.org/10.1016/0166-1280(90)85053-P.

(55) Dean, P. A. W. The Oxalate Dianion, $C_2O_4^{2-}$: Planar or Nonplanar? *J. Chem. Educ.* **2012**, *89* (3), 417–418. https://doi.org/10.1021/ed200202r.

(56) Zhou, G.; Li, W.-K. The Abnormally Long C-C Bond in the Oxalate Ion. *J. Chem. Educ.* **1989**, *66* (7), 572. https://doi.org/10.1021/ed066p572.

(57) Peterson, K. I.; Pullman, D. P. Determining the Structure of Oxalate Anion Using Infrared and Raman Spectroscopy Coupled with Gaussian Calculations. *J. Chem. Educ.* **2016**, *93* (6), 1130–1133. https://doi.org/10.1021/acs.jchemed.6b00118.

(58) Clark, R. J. H.; Firth, S. Raman, Infrared and Force Field Studies of $K_2{}^{12}C_2O_4 \cdot H_2O$ and $K_2{}^{13}C_2O_4 \cdot H_2O$ in the Solid State and in Aqueous Solution, and of $(NH_4)_2{}^{12}C_2O_4 \cdot H_2O$ and $(NH_4)_2{}^{13}C_2O_4 \cdot H_2O$ in the Solid State. *Spectrochim. Acta. A. Mol. Biomol. Spectrosc.* **2002**, *58* (8), 1731–1746. https://doi.org/10.1016/S1386-1425(01)00635-7.

(59) Begun, G. M.; Fletcher, W. H. Vibrational Spectra of Aqueous Oxalate Ion. *Spectrochim. Acta* **1963**, *19* (8), 1343–1349. https://doi.org/10.1016/0371-1951(63)80244-1.

(60) Kuroda, D. G.; Hochstrasser, R. M. Two-Dimensional Infrared Spectral Signature and Hydration of the Oxalate Dianion. *J. Chem. Phys.* **2011**, *135* (20). https://doi.org/10.1063/1.3658461.

(61) Kuroda, D. G.; Hochstrasser, R. M. Dynamic Structures of Aqueous Oxalate and the Effects of Counterions Seen by 2D IR. *Phys. Chem. Chem. Phys.* **2012**, *14* (18), 6219. https://doi.org/10.1039/c2cp23892f.

(62) Dinnebier, R. E.; Vensky, S.; Panthöfer, M.; Jansen, M. Crystal and Molecular Structures of Alkali Oxalates: First Proof of a Staggered Oxalate Anion in the Solid State. *Inorg. Chem.* **2003**, *42* (5), 1499–1507. https://doi.org/10.1021/ic0205536.

(63) Dinnebier, R. E.; Vensky, S.; Jansen, M.; Hanson, J. C. Crystal Structures and Topological Aspects of the High-Temperature Phases and Decomposition Products of the Alkali-Metal Oxalates $M_2[C_2O_4]$ (M=K, Rb, Cs). *Chem. – Eur. J.* **2005**, *11* (4), 1119–1129. https://doi.org/10.1002/chem.200400616.

(64) Reed, D. A.; Olmstead, M. M. Sodium Oxalate Structure Refinement. *Acta Crystallogr. B* **1981**, *37* (4), 938–939. https://doi.org/10.1107/S0567740881004676.

(65) Beagley, B.; Small, R. W. H. The Structure of Lithium Oxalate. *Acta Crystallogr.* **1964**, *17* (6), 783–788. https://doi.org/10.1107/S0365110X64002079.

(66) Fairley, D. A.; Scott, G. B. I.; Freeman, C. G.; Maclagan, R. G. A. R.; McEwan, M. J. C2H7O+ Potential Surface and Ion−Molecule Association between H3O+ and C2H4. *J. Phys. Chem. A* **1997**, *101* (15), 2848–2851. https://doi.org/10.1021/jp963294c.

(67) Dawson, P. H. A Study of the Collision-Induced Dissociation of $C_2H_5OH_2^+$ Using Various Target Gases. *Int. J. Mass Spectrom. Ion Phys.* **1983**, *50* (3), 287–297. https://doi.org/10.1016/0020-7381(83)87006-5.

(68) Graul, S. T.; Squires, R. R. Gas-Phase Acidities Derived from Threshold Energies for Activated Reactions. *J. Am. Chem. Soc.* **1990**, *112* (7), 2517–2529. https://doi.org/10.1021/ja00163a007.

(69) Menges, F. S.; Perez, E. H.; Edington, S. C.; Duong, C. H.; Yang, N.; Johnson, M. A. Integration of High-Resolution Mass Spectrometry with Cryogenic Ion Vibrational Spectroscopy. *J. Am. Soc. Mass Spectrom.* **2019**, *30* (9), 1551–1557. https://doi.org/10.1007/s13361-019-02238-y.

(70) Yang, N.; Duong, C. H.; Kelleher, P. J.; Johnson, M. A.; McCoy, A. B. Isolation of Site-Specific Anharmonicities of Individual Water Molecules in the I−·(H2O)2 Complex Using Tag-Free, Isotopomer Selective IR-IR Double Resonance. *Chem. Phys. Lett.* **2017**, *690*, 159–171. https://doi.org/10.1016/j.cplett.2017.09.042.

(71) Wolke, C. T.; DeBlase, A. F.; Leavitt, C. M.; McCoy, A. B.; Johnson, M. A. Diffuse Vibrational Signature of a Single Proton Embedded in the Oxalate Scaffold, $HO_2CCO_2^-$. *J. Phys. Chem. A* **2015**, *119* (52), 13018–13024. https://doi.org/10.1021/acs.jpca.5b10649.

(72) Frisch, M. J.; Trucks, G. W.; Schlegel, H. B.; Scuseria, G. E.; Robb, M. A.; Cheeseman, J. R.; Scalmani, G.; Barone, V.; Petersson, G. A.; Nakatsuji, H.; Li, X.; Caricato, M.; Marenich, A. V.; Bloino, J.; Janesko, B. G.; Gomperts, R.; Mennucci, B.; Hratchian, H. P.; Ortiz, J. V.; Izmaylov, A. F.; Sonnenberg, J. L.; Williams-Young, D.; Ding, F.; Lipparini, F.; Egidi, F.; Goings, J.; Peng, B.; Petrone, A.; Henderson, T.; Ranasinghe, D.; Zakrzewski, V. G.; Gao, J.; Rega, N.; Zheng, G.; Liang, W.; Hada, M.; Ehara, M.; Toyota, K.; Fukuda, R.; Hasegawa, J.; Ishida, M.; Nakajima, T.; Honda, Y.; Kitao, O.; Nakai, H.; Vreven, T.; Throssell, K.; Montgomery, J. A., Jr; Peralta, J. E.; Ogliaro, F.; Bearpark, M.; Heyd, J. J.; Brothers, E.; Kudin, K. N.; Staroverov, V. N.; Keith, T. A.; Kobayashi, R.; Normand, J.; Raghavachari, K.; Rendell, A.; Burant, J. C.;

Iyengar, S. S.; Tomasi, J.; Cossi, M.; Milliam, J. M.; Klene, M.; Adamo, C.; Cammi, R.; Ochterski, J. W.; Martin, R. L.; Morokuma, K.; Farkas, O.; Foresman, J. B.; Fox, D. J. Gaussian 16, Revision A. 03, Gaussian. *Inc Wallingford CT* **2016**.

(73) Becke, A. D. Density-Functional Exchange-Energy Approximation with Correct Asymptotic Behavior. *Phys. Rev. A* **1988**, *38* (6), 3098–3100. https://doi.org/10.1103/PhysRevA.38.3098.

(74) Lee, C.; Yang, W.; Parr, R. G. Development of the Colle-Salvetti Correlation-Energy Formula into a Functional of the Electron Density. *Phys. Rev. B* **1988**, *37* (2), 785–789. https://doi.org/10.1103/PhysRevB.37.785.

(75) Curtiss, L. A.; Redfern, P. C.; Raghavachari, K. Gaussian-4 Theory. *J. Chem. Phys.* **2007**, *126* (8), 084108. https://doi.org/10.1063/1.2436888.

(76) Curtiss, L. A.; Redfern, P. C.; Raghavachari, K. Assessment of Gaussian-4 Theory for Energy Barriers. *Chem. Phys. Lett.* **2010**, *499* (1–3), 168–172. https://doi.org/10.1016/j.cplett.2010.09.012.

(77) Møller, Chr.; Plesset, M. S. Note on an Approximation Treatment for Many-Electron Systems. *Phys. Rev.* **1934**, *46* (7), 618–622. https://doi.org/10.1103/PhysRev.46.618.

(78) Valiev, M.; Bylaska, E. J.; Govind, N.; Kowalski, K.; Straatsma, T. P.; Van Dam, H. J. J.; Wang, D.; Nieplocha, J.; Apra, E.; Windus, T. L.; de Jong, W. A. NWChem: A Comprehensive and Scalable Open-Source Solution for Large Scale Molecular Simulations. *Comput. Phys. Commun.* **2010**, *181* (9), 1477–1489. https://doi.org/10.1016/j.cpc.2010.04.018.

(79) Čížek, J. On the Correlation Problem in Atomic and Molecular Systems. Calculation of Wavefunction Components in Ursell-Type Expansion Using Quantum-Field Theoretical Methods. *J. Chem. Phys.* **1966**, *45* (11), 4256–4266. https://doi.org/10.1063/1.1727484.

(80) Purvis, G. D.; Bartlett, R. J. A Full Coupled-cluster Singles and Doubles Model: The Inclusion of Disconnected Triples. *J. Chem. Phys.* **1982**, *76* (4), 1910–1918. https://doi.org/10.1063/1.443164.

(81) Pople, J. A.; Head-Gordon, M.; Raghavachari, K. Quadratic Configuration Interaction. A General Technique for Determining Electron Correlation Energies. *J. Chem. Phys.* **1987**, *87* (10), 5968–5975. https://doi.org/10.1063/1.453520.

(82) Rassolov, V. A.; Pople, J. A.; Redfern, P. C.; Curtiss, L. A. The Definition of Core Electrons. *Chem. Phys. Lett.* **2001**, *350* (5–6), 573–576. https://doi.org/10.1016/S0009-2614(01)01345-8.

(83) Petrie, S. Pitfalls for the Frozen-Core Approximation: Gaussian-2 Calculations on the Sodium Cation Affinities of Diatomic Fluorides. *J. Phys. Chem. A* **1998**, *102* (30), 6138–6151. https://doi.org/10.1021/jp9802432.

(84) Schuchardt, K. L.; Didier, B. T.; Elsethagen, T.; Sun, L.; Gurumoorthi, V.; Chase, J.; Li, J.; Windus, T. L. Basis Set Exchange: A Community Database for Computational Sciences. *J. Chem. Inf. Model.* **2007**, *47* (3), 1045–1052. https://doi.org/10.1021/ci600510j.

(85) Pritchard, B. P.; Altarawy, D.; Didier, B.; Gibson, T. D.; Windus, T. L. New Basis Set Exchange: An Open, Up-to-Date Resource for the Molecular Sciences Community. *J. Chem. Inf. Model.* **2019**, *59* (11), 4814–4820. https://doi.org/10.1021/acs.jcim.9b00725.

(86) Feller, D. The Role of Databases in Support of Computational Chemistry Calculations. *J. Comput. Chem.* **1996**, *17* (13), 1571–1586. https://doi.org/10.1002/(SICI)1096-987X(199610)17:13<1571::AID-JCC9>3.0.CO;2-P.

(87) Weigend, F.; Ahlrichs, R. Balanced Basis Sets of Split Valence, Triple Zeta Valence and Quadruple Zeta Valence Quality for H to Rn: Design and Assessment of Accuracy. *Phys. Chem. Chem. Phys.* **2005**, *7* (18), 3297. https://doi.org/10.1039/b508541a.

(88) Rappoport, D.; Furche, F. Property-Optimized Gaussian Basis Sets for Molecular Response Calculations. *J. Chem. Phys.* **2010**, *133* (13), 134105. https://doi.org/10.1063/1.3484283.

(89) Kaupp, M.; Schleyer, P. v. R.; Stoll, H.; Preuss, H. Pseudopotential Approaches to Ca, Sr, and Ba Hydrides. Why Are Some Alkaline Earth MX_2 Compounds Bent? *J. Chem. Phys.* **1991**, *94* (2), 1360–1366. https://doi.org/10.1063/1.459993.

(90) Boys, S. F.; Bernardi, F. The Calculation of Small Molecular Interactions by the Differences of Separate Total Energies. Some Procedures with Reduced Errors. *Mol. Phys.* **1970**, *19* (4), 553–566. https://doi.org/10.1080/00268977000101561.

(91) Simon, S.; Duran, M.; Dannenberg, J. J. How Does Basis Set Superposition Error Change the Potential Surfaces for Hydrogen-bonded Dimers? *J. Chem. Phys.* **1996**, *105* (24), 11024–11031. https://doi.org/10.1063/1.472902.

(92) van Duijneveldt, F. B.; van Duijneveldt-van de Rijdt, J. G. C. M.; van Lenthe, J. H. State of the Art in Counterpoise Theory. *Chem. Rev.* **1994**, *94* (7), 1873–1885. https://doi.org/10.1021/cr00031a007.

(93) Xantheas, S. S. On the Importance of the Fragment Relaxation Energy Terms in the Estimation of the Basis Set Superposition Error Correction to the Intermolecular Interaction Energy. *J. Chem. Phys.* **1996**, *104* (21), 8821–8824. https://doi.org/10.1063/1.471605.

(94) Dollimore, D.; Tinsley, D. The Thermal Decomposition of Oxalates. Part XII. The Thermal Decomposition of Lithium Oxalate. *J. Chem. Soc. Inorg. Phys. Theor.* **1971**, *0* (0), 3043–3047. https://doi.org/10.1039/J19710003043.

(95) Ito, R.; Masuda, Y.; Ito, Y. Thermal Analyses of Rubidium and Cesium Oxalate Monohydrates. *Thermochim. Acta* **1988**, *127*, 159–170. https://doi.org/10.1016/0040-6031(88)87492-6.

(96) Kahwa, I. A.; Mulokozi, A. M. The Thermal Decomposition Temperatures of Ionic Metal Oxalates. *J. Therm. Anal.* **1981**, *22* (1), 61–65. https://doi.org/10.1007/BF01915696.

(97) Higashiyama, T.; Hasegawa, S. The Differential Thermal Analysis of Potassium Oxalate. *Bull. Chem. Soc. Jpn.* **1971**, *44* (7), 1727–1730. https://doi.org/10.1246/bcsj.44.1727.

(98) Haeffler, G.; Hanstorp, D.; Kiyan, I.; Klinkmüller, A. E.; Ljungblad, U.; Pegg, D. J. Electron Affinity of Li: A State-Selective Measurement. *Phys. Rev. A* **1996**, *53* (6), 4127–4131. https://doi.org/10.1103/PhysRevA.53.4127.

(99) Hotop, H.; Lineberger, W. C. Binding Energies in Atomic Negative Ions: II. *J. Phys. Chem. Ref. Data* **1985**, *14* (3), 731–750. https://doi.org/10.1063/1.555735.

(100) Andersson, K. T.; Sandström, J.; Kiyan, I. Yu.; Hanstorp, D.; Pegg, D. J. Measurement of the Electron Affinity of Potassium. *Phys. Rev. A* **2000**, *62* (2), 022503. https://doi.org/10.1103/PhysRevA.62.022503.

(101) Frey, P.; Breyer, F.; Holop, H. High Resolution Photodetachment from the Rubidium Negative Ion around the Rb(5p1/2) Threshold. *J. Phys. B At. Mol. Phys.* **1978**, *11* (19), L589–L594. https://doi.org/10.1088/0022-3700/11/19/005.

(102) Scheer, M.; Thøgersen, J.; Bilodeau, R. C.; Brodie, C. A.; Haugen, H. K.; Andersen, H. H.; Kristensen, P.; Andersen, T. Experimental Evidence That the $6s6p^3$ States of Cs^- Are Shape Resonances. *Phys. Rev. Lett.* **1998**, *80* (4), 684–687. https://doi.org/10.1103/PhysRevLett.80.684.

(103) Andersen, T. Atomic Negative Ions: Structure, Dynamics and Collisions. *Phys. Rep.* **2004**, *394* (4), 157–313. https://doi.org/10.1016/j.physrep.2004.01.001.

(104) Pathak, H.; Sasmal, S.; Nayak, M. K.; Vaval, N.; Pal, S. Relativistic Equation-of-Motion Coupled-Cluster Method for the Electron Attachment Problem. *Comput. Theor. Chem.* **2016**, *1076*, 94–100. https://doi.org/10.1016/j.comptc.2015.12.015.

(105) Salomonson, S.; Warston, H.; Lindgren, I. Many-Body Calculations of the Electron Affinity for Ca and Sr. *Phys. Rev. Lett.* **1996**, *76* (17), 3092–3095. https://doi.org/10.1103/PhysRevLett.76.3092.

(106) Tellgren, R.; Olovsson, I. Hydrogen Bond Studies. XXXXVI. The Crystal Structures of Normal and Deuterated Sodium Hydrogen Oxalate Monohydrate $NaHC_2O_4{\cdot}H_2O$ and $NaDC_2O_4{\cdot}D_2O$. *J. Chem. Phys.* **1971**, *54* (1), 127–134. https://doi.org/10.1063/1.1674582.

(107) Pedersen, B. F. The Crystal Structure of Potassium Hydrogen Oxalate. *Acta Chem Scand* **1968**, *22* (9).

(108) Einspahr, H.; Marsh, R. E.; Donohue, J. The Crystal Structure of Potassium Binoxalate. *Acta Crystallogr. B* **1972**, *28* (7), 2194–2198. https://doi.org/10.1107/S0567740872005783.

(109) Kholodkovskaya, L. N.; Trunov, V. K.; Tskhelashvili, N. B. Refinement of the Crystal Structures of Potassium and Rubidium Hydrogen Oxalates MHC_2O_4 (M=K, Rb). *J. Struct. Chem.* **1990**, *31* (3), 509–511. https://doi.org/10.1007/BF00743603.

(110) Liu, G.; Ciborowski, S. M.; Zhu, Z.; Chen, Y.; Zhang, X.; Bowen, K. H. The Metallo-Formate Anions, M(CO2)−, M = Ni, Pd, Pt, Formed by Electron-Induced CO2 Activation. *Phys. Chem. Chem. Phys.* **2019**, *21* (21), 10955–10960. https://doi.org/10.1039/C9CP01915D.

(111) Knurr, B. J.; Weber, J. M. Solvent-Driven Reductive Activation of Carbon Dioxide by Gold Anions. *J. Am. Chem. Soc.* **2012**, *134* (45), 18804–18808. https://doi.org/10.1021/ja308991a.

(112) Kepp, K. P. A Quantitative Scale of Oxophilicity and Thiophilicity. *Inorg. Chem.* **2016**, *55* (18), 9461–9470. https://doi.org/10.1021/acs.inorgchem.6b01702.

(113) Glendening, E. D.; Reed, A. E.; Carpenter, J. E.; Weinhold, F. *NBO Version 3.1*.

(114) Zhou, M.; Andrews, L. Infrared Spectra of the CO_2^- and $C_2O_4^-$ Anions Isolated in Solid Argon. *J. Chem. Phys.* **1999**, *110* (5), 2414–2422. https://doi.org/10.1063/1.477947.

(115) Gordon, A. J.; Ford, R. A. *The Chemist's Companion: A Handbook of Practical Data, Techniques, and References*; Wiley: New York, 1972.

(116) Saethre, L. J.; Thomas, T. D. On the Origin of Substituent Effects in Electrophilic Addition: Evidence from Core-Electron Spectroscopy. *J. Org. Chem.* **1991**, *56* (12), 3935–3942. https://doi.org/10.1021/jo00012a029.

(117) Fernández, I.; Frenking, G.; Uggerud, E. Rate-Determining Factors in Nucleophilic Aromatic Substitution Reactions. *J. Org. Chem.* **2010**, *75* (9), 2971–2980. https://doi.org/10.1021/jo100195w.